

Damping effect on transverse flow-induced vibration of a rotating circular cylinder and its implied energy harvesting performance

Jisheng Zhao ^{*}, Mark C. Thompson , and Kerry Hourigan 

Fluids Laboratory for Aeronautical and Industrial Research (FLAIR), Department of Mechanical and Aerospace Engineering, Monash University, Clayton, Victoria 3800, Australia



(Received 24 September 2021; accepted 1 February 2022; published 17 February 2022)

This study experimentally investigates the effect of structural damping on the transverse flow-induced vibration (FIV) of an elastically mounted circular cylinder under imposed axial rotation in a free stream. It has been shown by Wong *et al.* [K. W. L. Wong, J. Zhao, D. Lo Jacono, M. C. Thompson, and J. Sheridan, *J. Fluid Mech.* **829**, 486 (2017)] that FIV of a circular cylinder can be enhanced or attenuated by imposing an axial rotation. Here, we demonstrate that the rotation-enhanced FIV response is more susceptible to the varying damping than the nonrotating cylinder. The rotation-enhanced response diminishes when the damping ratio is increased to a certain value for the fixed rotation rate of $\alpha = 2.0$ ($\alpha =$ cylinder surface to free-stream velocity). We also analyze the forcing components, showing that the time-averaged lift coefficient is predominantly dependent on the rotation rate over the Reynolds number range ($1130 \leq \text{Re} \leq 5260$) tested. Interestingly, it emerges that the FIV of a rotating cylinder is associated with harmonic force components and wake modes different than those of the nonrotating cylinder, despite the existence of a similar three-branch response. In terms of the implication for energy harvesting, we demonstrate a 33% increase in the peak power output compared with the nonrotating cylinder, noting that enhancement occurs within the range $1.5 \leq \alpha \leq 2.0$.

DOI: [10.1103/PhysRevFluids.7.023905](https://doi.org/10.1103/PhysRevFluids.7.023905)

I. INTRODUCTION

Flow-induced vibration (FIV) is a subject of great interest in the field of fluid-structure interaction, due to its intrinsic dynamics that are of scientific interest and significant implications in a wide variety of engineering areas. Since the pioneering experiments of Brooks [1], the two-sided roles of FIV, being both an undesirable phenomenon in practical engineering and a potential renewable energy harvesting source (e.g., Refs. [2–5]), have increasingly motivated ongoing research that aims to model, characterize, predict, and control FIV (e.g., Refs. [6–9]).

Fundamentally, there are two body-oscillator phenomena typical of FIV: *vortex-induced vibration (VIV)* and *galloping*. VIV is caused by vortices shed periodically from an elastic or elastically mounted body, and thus it is self-limited by the vortex-shedding process. On the other hand, galloping, known as an aeroelastic instability, is driven by the unsteady aerodynamic forces arising from an asymmetric pressure distribution around the body that is induced by changes in relative incidence angle when the body moves in the flow. Studies have demonstrated that, depending on the flow velocity and structural properties (e.g., the geometry, afterbody, mass ratio, and damping), the two body-oscillator phenomena may occur separately or concurrently, resulting in profound dynamics of fluid-structure interaction (see Refs. [10–13]). In the present study, the focus is on the

*jisheng.zhao@monash.edu

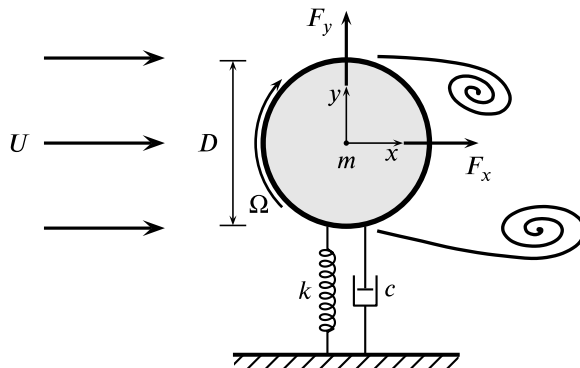


FIG. 1. Definition sketch for transverse flow-induced vibration of a rotating cylinder. The axis of rotation is perpendicular to the x - y plane. U is the free-stream velocity, D the cylinder diameter, m the oscillating mass, k the spring constant, c the structural damping, and Ω the angular velocity. F_y represents the transverse (lift) force components acting on the body. The angular rotation speed is represented by Ω , with its positive direction in the clockwise direction that generates a positive Magnus force.

effect of structural damping on the FIV of a circular cylinder with an imposed rotation to break the axial symmetry of the fluid-structure system for control purposes.

In the past century, flow past a rotating cylinder has been extensively investigated to examine the effect of imposed rotation on fluid forces (i.e., lift augmentation due to the *Magnus effect*, named after the well-known physicist G. Magnus who first demonstrated this phenomenon in experiments in 1852), and wake structures (see Refs. [14–18]). It has been found that the fluid forces and wake structures are dependent on both the Reynolds number $Re = UD/\nu$ and the dimensionless rotation rate $\alpha = \Omega D/(2U)$, where U is the free-stream velocity, ν is the kinematic viscosity of the fluid, D is the cylinder diameter, and Ω is the angular velocity of rotation, as illustrated in Fig. 1.

More recently, the rotation effect has been adopted for active control of FIV of circular cylinders [19–26], and spheres [27–29]. In particular, Wong *et al.* [19] have examined the FIV response of a rotating cylinder over a wide parameter space of reduced velocity and rotation rate, showing that the three amplitude branches (namely, the initial, upper, and lower branches coined by Khalak and Williamson [6]) typical of VIV of a circular cylinder with low mass and damping ratios can be enhanced significantly ($\sim 80\%$ in the peak amplitude) by the imposed rotation up to $\alpha \approx 2.3$, prior to an abrupt substantial reduction or even full suppression for higher α values. Note that here the reduced velocity is defined by $U^* = U/(f_{nw}D)$, where f_{nw} is the natural frequency of the system in quiescent water. They have also demonstrated a variety of wake patterns and complicated switching behaviors of wake modes occurring on a U^* - α map. However, the fluid forcing components remain largely unknown in their study.

On the other hand, the damping effect on VIV of a low-mass-ratio circular cylinder has been investigated experimentally by Soti *et al.* [4]. They showed that the existence of the upper branch continued with a peak amplitude down to $0.2D$ as the structural damping ratio was increased. The implicated maximum average power output coefficient was found to be 0.151 – 0.200 in the Reynolds number range of 1750 – 5330 . It is suggested that the energy harvesting performance improves with increasing Re .

Following on from Wong *et al.* [19] and Soti *et al.* [4], the present study investigates the combined effect of rotation and damping on FIV of a circular cylinder. We aim to gain a deeper understanding of how the three-branch amplitude response enhanced by imposed rotation is attenuated or suppressed by structural damping. More generally, this study characterizes the dynamics and wake structures over a parameter space across wide ranges of reduced velocity, rotation rate, and damping ratio. To provide insight into the mechanism of fluid-structure interaction, we present a

detailed frequency analysis for the structural vibration and the driving fluid forces, while wake structures associated with different FIV response regimes are also discussed. Of interest, the implied energy harvesting performance of a rotating cylinder is assessed by comparing with its nonrotating counterpart.

II. EXPERIMENTAL METHODOLOGY

A. Fluid-structure system modeling

The fluid-structure system is modeled as a single-degree-of-freedom mass-spring-damper oscillator subjected to a fluid flow, as sketched in Fig. 1. The elastically mounted cylinder is free to oscillate only in the cross-flow direction to the oncoming free-stream. The body dynamics is governed by a linear second-order oscillator equation:

$$m\ddot{y}(t) + c\dot{y}(t) + ky(t) = F_y(t), \quad (1)$$

where m is the total oscillating mass of the system, c is the structural damping, k is the spring constant, $y(t)$ is the body displacement, and $F_y(t)$ represents the transverse fluid force (the lift). Note that the transverse fluid force coefficient used in this study is defined by $C_y = F_y/(\frac{1}{2}\rho U^2 DL)$, where ρ is the fluid density and L is the cylinder immersed span.

In the present study, the experimental modeling was based on a low-friction air-bearing system in conjunction with a recirculating free-surface water channel of the Fluids Laboratory for Aeronautical and Industrial Research (FLAIR) at Monash University. Details of the air-bearing system and water channel facilities have been described in the previous related studies of Wong *et al.* [24] and Zhao *et al.* [25]. Figure 2 shows photographs to clarify key components of the present experimental rig. The air-bearing system was placed atop and aligned transverse to the water channel. The test cylinder coupled with a stepper motor rig was vertically adapted to the air-bearing slider carriage that was guided by precision stainless steel shafts to provide linear movement. The rigid cylinder model, precision-made from aluminium tubing, had an outer diameter of $D = 30 \pm 0.01$ mm. The immersed length of cylinder was $L = 614$ mm, yielding a span-to-diameter aspect ratio of $AR = L/D = 20.5$. To reduce end effects of the cylinder and to promote parallel vortex shedding, an end conditioning platform was used (for more details, see Refs. [24,25]). The total oscillating mass of the system was $m = 2630.6$ g, and the displaced mass of water was $m_d = \rho\pi D^2 L/4 = 433.6$ g, giving a mass ratio of $m^* = m/m_d = 6.07$.

An eddy-current-based damping mechanism was used to control the structural damping by varying the damper gap via a micro-drive stage with a resolution of 0.01 mm [see Fig. 2(c)]. Details of the design of this damper device can be found in Ref. [4]. The structural stiffness of the mass-spring-damper system was controlled by precision extension springs. Free decay tests were conducted individually in air and in quiescent water to determine the structural damping ratio and the natural frequency of the system in each scenario. Figure 3 shows the free decay test results of the structural damping ratios (i.e., ζ_a in air and ζ with consideration of the added mass) and the natural frequencies (i.e., f_{na} in air and f_{nw} in quiescent water) as a function of the damper gap (G , in mm). Note that the structural damping ratio with consideration of the added mass was given by $\zeta = c/2\sqrt{k(m + m_A)}$, where the added mass, given by $m_A = [(f_{na}/f_{nw})^2 - 1]m$, was found to be 471.3 g, while the added mass coefficient, defined by $C_A = m_A/m_d$, was found to be 1.09. As shown in Fig. 3, the structural damping ratio varied nonlinearly with the damper gap (close to an exponentially decreasing trend with increasing G); on the other hand, the natural frequencies both in air and in quiescent water remained consistent, i.e., $f_{na} = 0.455$ Hz and $f_{nw} = 0.419$ Hz, with decreasing damper gap until $G < 2$ when structural damping effects became sufficiently strong to affect the natural frequencies.

The imposed cylinder rotation was driven by a miniature stepper motor (Model LV172, Parker Hannifin, USA) that was controlled by a micro-stepping drive (Model: E-DC) with a resolution

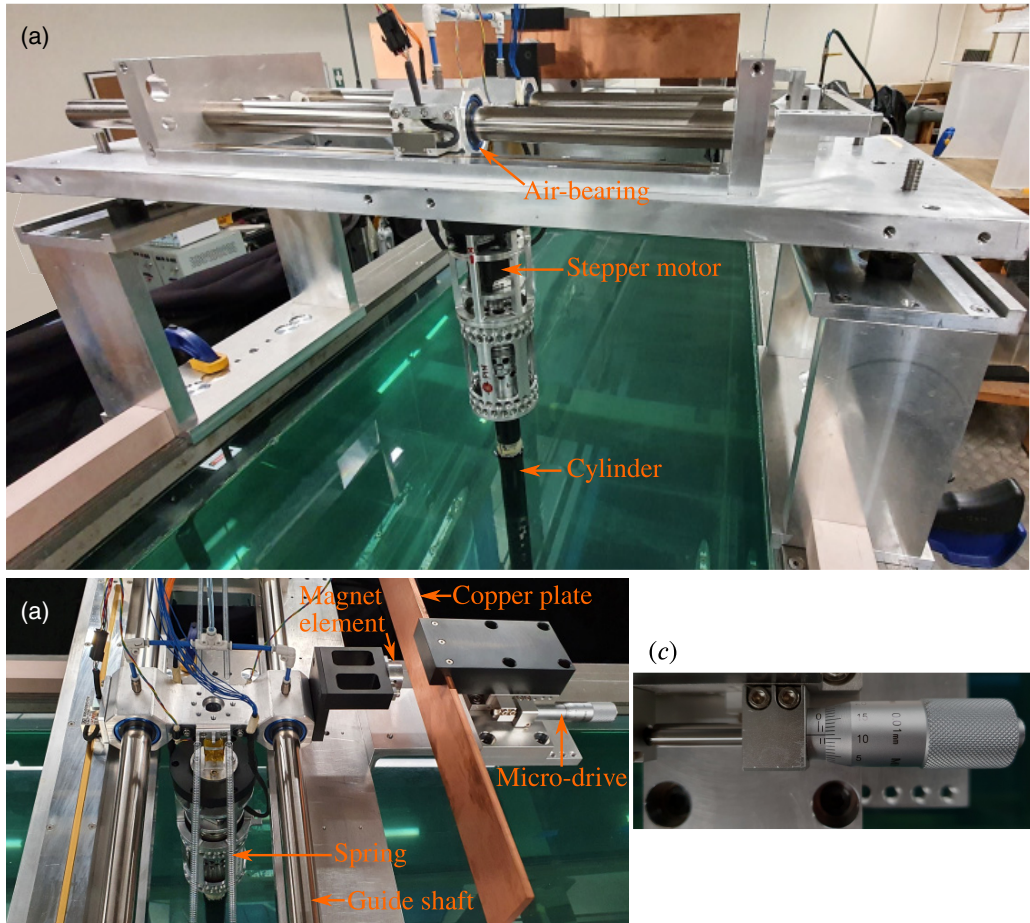


FIG. 2. Photographs showing the experimental setup in (a) the front view and (b) the top view, where key components of the air-bearing system, the rotation rig, and the damper device are illustrated. Panel (c) shows a close-up view of the micro-drive used to control the damper gap.

of 25 000 steps per revolution and a Parker 6K2 motion controller. More details of this motor mechanism can be found in Refs. [24,25].

B. Data acquisition and processing methods

The data acquisition and the control of the free-stream velocity and the motor rotary motion were automated using a workstation computer equipped with customized LABVIEW (National Instruments, USA) programs. The reduced velocity was varied over the range of $3 \leq U^* \leq 13$ in increments between 0.1 and 0.2 (depending on structural response regimes). The Reynolds number range was $1130 \leq Re \leq 5260$, with a relative uncertainty of 1%. Note that the experimental data sets were collected in a consistent manner with increasing reduced velocities for fixed rotation rates or with increasing rotation rates for fixed reduced velocities.

The body displacement and the fluid forces acting on the cylinder were measured simultaneously. The body displacement was measured using a noncontact digital optical linear encoder (Model RGH24, Renishaw, UK). This linear encoder had a resolution of $1 \mu\text{m}$ and a linear range of ± 200 mm available. An optical rotary encoder with a resolution of 4000 counts per revolution (Model

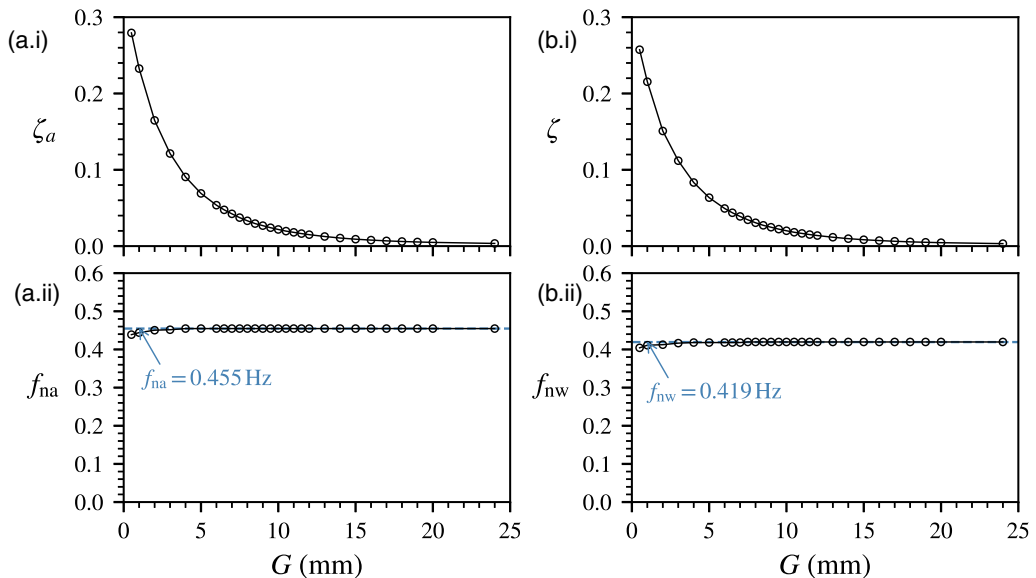


FIG. 3. Free decay test results of the structural damping ratios and natural frequencies as a function of the damper gap. Panels (a.i) and (a.ii) show the results of the structural damping ratio (ζ_a) and the natural frequency (f_{na}) in air, respectively, while panels (b.i) and (b.ii) show the structural damping ratio with the consideration of added mass (ζ) and the natural frequency (f_{nw}) in quiescent water, respectively.

E5-1000, US Digital, USA) was used to measure the rotary motion [25]. The transverse fluid force (the lift, F_y) was determined based on Eq. (1). The force measurement technique has been detailed and validated in Refs. [9, 11, 25, 27, 28]. The water temperature was measured using a platinum-based resistance temperature detector in conjunction with a Pt100 converter (Model 3112, PR Electronics, USA). This temperature converter had an accuracy of 0.05% for the configured range of 10-40 °C. For each measurement case, the data acquisition was made at a sampling frequency of 100 Hz for 300 s, which could obtain data from more than 140 vibration cycles for analysis.

To visualize the flow structure associated with the cylinder dynamic response, the near wake of the cylinder was examined using the particle image velocimetry (PIV) technique. The PIV system used has been detailed in the previous study of Zhao *et al.* [12, 25].

More details of the experimental validation can be found in the studies of Wong *et al.* [24] and Zhao *et al.* [25].

III. RESULTS AND DISCUSSION

A. Dynamical response as a function of reduced velocity

In this subsection, we examine the damping effect on the FIV response of a rotating cylinder at $\alpha = 2.0$ as a function of reduced velocity. The selection of this α value was based on the previous study of Wong *et al.* [19] showing that the largest vibration amplitudes occurred at $\alpha \simeq 2.0$, prior to an abrupt decrease in the amplitude response at $\alpha \simeq 2.3$ for the upper branch.

Figure 4 shows the variations of the normalized body vibration amplitude (A_{10}^*) as a function of reduced velocity for $\alpha = 2.0$ with a wide range of structural damping ratios, as compared with selected cases of the nonrotating cylinder ($\alpha = 0$). Note that A_{10}^* represents the mean of the top 10% amplitude peaks normalized by the cylinder diameter D (for each U^*). As can be seen in Fig. 4(a), for the lowest damping ratio case ($\zeta = 0.0032$, $G = 24.00$ mm), the maximum A_{10}^* is observed to be 1.32 in the upper branch, a 69% increase over its nonrotating counterpart. This amplitude increase is somewhat lower than the 80% reported by Wong *et al.* [19], and it could be

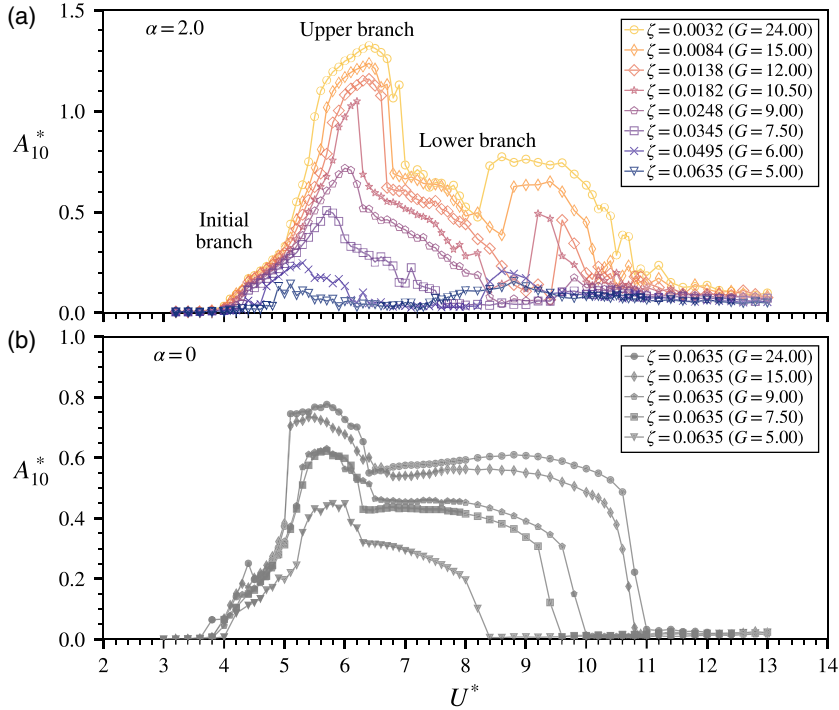


FIG. 4. The normalized amplitude (A_{10}^*) as a function of U^* at the imposed rotation speed ratio of $\alpha = 2.0$ with various damping ratios, as compared with selected nonrotating cases ($\alpha = 0$).

attributable to the differences in mass ratios between the two studies (i.e., $m^* = 5.78$ in Ref. [19]). As ζ is increased gradually to 0.0248 ($G = 9.50$ mm), the initial to upper branch jump diminishes, and the amplitude response becomes “two-branched” with a seemingly continuous branch growth up to $U^* = 6$ prior to sharply dropping to the lower branch. For this ζ case, the maximum vibration amplitude is found to be $A_{10}^* = 0.72$, a 14% increase over its nonrotating counterpart. With ζ further increased to 0.0345 ($G = 7.50$ mm), the vibration amplitudes appear to be lower than those of its nonrotating counterpart; in other words, at $\alpha = 2.0$, the cylinder rotation exhibits an attenuation effect in this ζ case. On the other hand, the amplitude peak is reduced to $A_{10}^* = 0.51$, a decrease of 60% from that of the lowest ζ case. This reduction ratio is substantially greater than the 20% for the nonrotating counterpart. Unexpectedly, for a further higher damping ratio of $\zeta = 0.0635$ ($G = 5.00$ mm), the rotating cylinder sees FIV suppression for the entire U^* range tested, while its nonrotating counterpart still displays a significant FIV response.

In particular, the lower branch for the rotating cases appears to be sensitive to changes in ζ , as reflected by a V-shape drop at $U^* \approx 8$, whereas all nonrotating cases display a well-defined lower branch profile. In fact, this V-shape drop is associated with the loss of body-wake synchronization, as revealed in the frequency power spectra density contour plots in Fig. 5. As can be seen in Fig. 5(b.ii), the lower branch for $\zeta = 0.0032$ is associated with a second harmonic in the lift frequency response ($f_{C_y}^*$), whereas the nonrotating counterpart displays a third harmonic [Fig. 5(b.i)]. The fluid forcing frequency response was not examined previously by Wong *et al.* [19]; however, Zhao *et al.* [25] showed a secondary harmonic clearly existing in $f_{C_y}^*$ when significant body-wake synchronization was encountered in inline FIV of a rotating cylinder. Thus, the difference in the frequency components between the rotating and nonrotating cases can be linked to different vortex-shedding modes. More discussion on wake modes is given in Sec. III C. As ζ is increased, the lower branch sees an interrupted region of desynchronization [e.g., $\zeta = 0.0182$, $G = 10.50$ mm

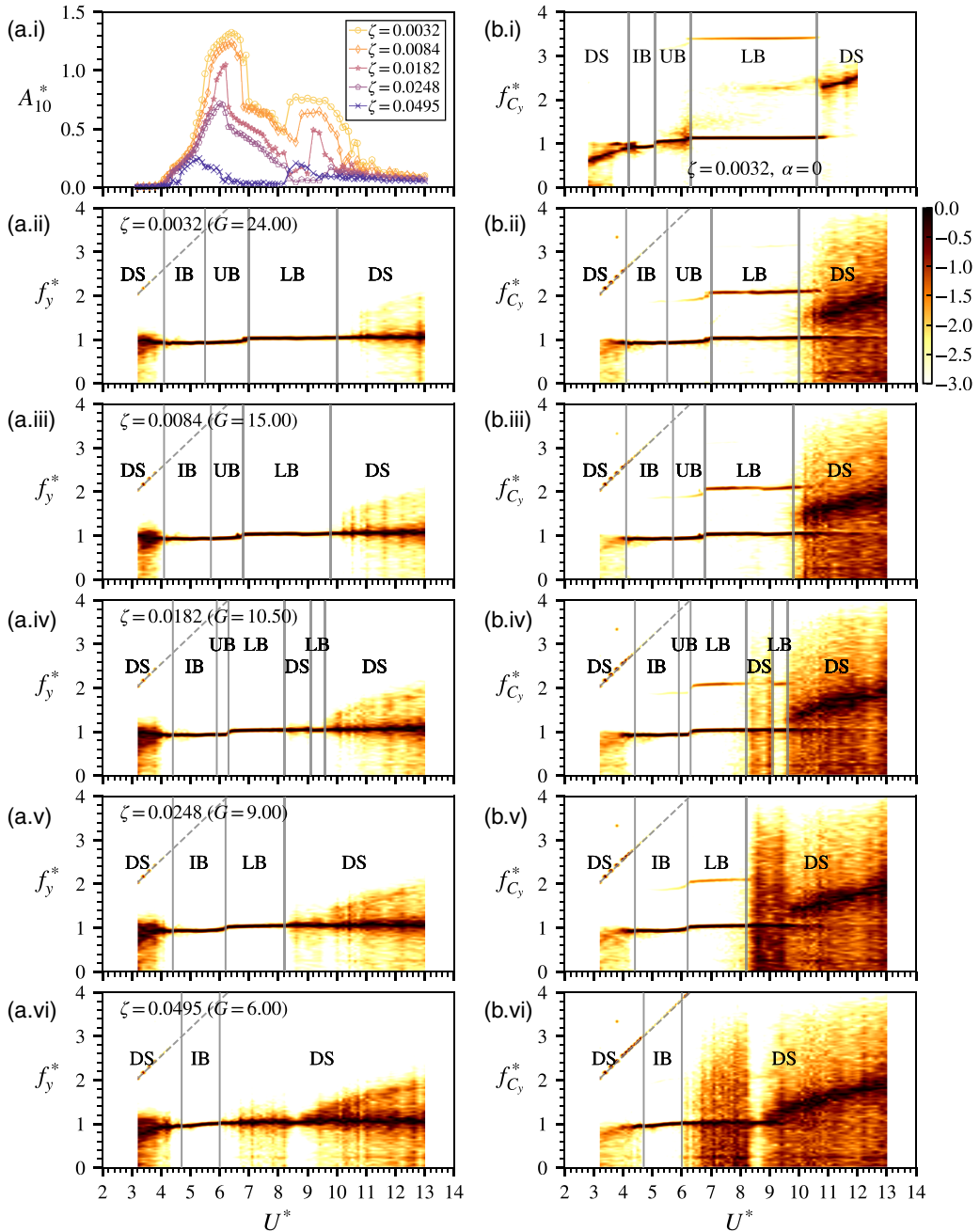


FIG. 5. Normalized amplitude and frequency responses as a function of the reduced velocity at $\alpha = 2.0$ with various selected damping ratios. Note that the normalized frequencies are given by $f^* = f/f_{nw}$, and their power spectral densities are logarithmic scaled. The dashed slope line represents the normalized rotation frequency $\alpha U^*/\pi$. For comparison of $f_{C_y}^*$, panel (b.i) shows the case of $\alpha = 0$ and $\zeta = 0.0032$. The vertical lines separate the FIV response regimes of the initial branch (IB), the upper branch (UB), the lower branch (LB), and desynchronization (DS).

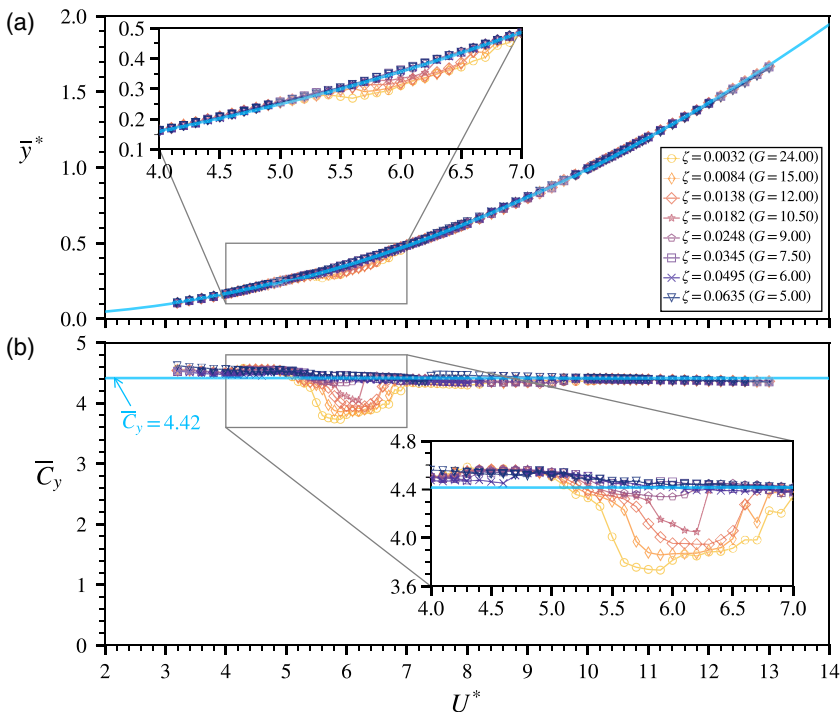


FIG. 6. Time-averaged displacement (\bar{y}^*) and time-averaged lift coefficient (\bar{C}_y) as a function of U^* at the imposed rotation speed ratio of $\alpha = 2.0$ with various damping ratios. In panel (a), the blue solid line represents the second-order polynomial fit curve through all measurement cases, while in panel (b) the blue solid line represents the averaged value of all \bar{C}_y values.

in Fig. 5(b.iv)] corresponding to a V-shape drop in the A_{10}^* response. However, it is unclear why this desynchronization occurs in the middle of the lower branch, where strong fluid-structure interaction would be expected to result in a body-wake synchronization. Nevertheless, the above results suggest that the FIV response of a rotating cylinder is more susceptible to the damping effect than its nonrotating counterpart.

Furthermore, we examine the damping effect on the time-averaged cylinder position and the lift force coefficient. Figure 6 shows the time-averaged body position (\bar{y}^*) and time-averaged transverse fluid force coefficient (\bar{C}_y) for the test cases of $\alpha = 2.0$. Note that \bar{y}^* represents the normalized time-averaged of the cylinder displacement from its neutral position at zero flow velocity, i.e., $\bar{y}^* = \bar{y}/D$. Following the analytical approach used in the inline FIV case by Zhao *et al.* [25], by taking the temporal average of both sides of Eq. (1), the time-averaged cylinder displacement can be given by

$$\bar{y} = \frac{\bar{F}_y}{k}, \quad (2)$$

and its dimensionless form (normalized by the cylinder diameter D) is determined by

$$\bar{y}^* = \frac{\rho U^2 L \bar{C}_y}{2k}. \quad (3)$$

Then, substituting for $U^* = U/(f_{\text{nw}}D)$ and $k \cong (2\pi f_{\text{na}})^2 m$ gives

$$\bar{y}^* = \frac{\rho (U^* f_{\text{nw}} D)^2 L \bar{C}_y}{2(2\pi f_{\text{na}})^2 m}, \quad (4)$$

and, with $m_d = \rho\pi D^2L/4$ and $C_A = m_A/m_d = [(f_{na}/f_{nw})^2 - 1]m^*$, Eq. (4) can be rewritten by

$$\bar{y}^* = \frac{U^{*2}\bar{C}_y}{2\pi^3(C_A + m^*)}. \quad (5)$$

Clearly, \bar{y}^* depends on U^* and \bar{C}_y for given C_A and m^* . As shown in Fig. 4(b), \bar{y}^* increases parabolically with U^* . Based on Eq. (5), this implies that \bar{C}_y is likely to be independent of U^* . As shown in Fig. 4(c), for a given rotation rate (i.e., $\alpha = 2.0$), \bar{C}_y remains almost constant at 4.42 (represented by a blue solid line) for almost the entire U^* range tested, except for $4 \lesssim U^* \lesssim 7$ covering the initial and upper branches, where \bar{C}_y deviates from the average value for all damped cases. On the other hand, \bar{y}^* also deviates from its parabolic increase trend over $5.5 < U^* < 6.5$ in the upper-branch regime. The deviations in \bar{y}^* and \bar{C}_y are attributable to strong fluid-structure interaction associated with large-amplitude oscillations, as explained for the inline FIV case by Zhao *et al.* [25]. The above results indicate that, perhaps unsurprisingly, damping in general has marginal influence on the Magnus force coefficient (i.e., \bar{C}_y) experienced by a rotating cylinder undergoing transverse FIV. In fact, \bar{C}_y depends predominantly on α in the Reynolds number range tested in the present study, which is further discussed in Sec. III B.

Moreover, we assess the fluid-flow energy harvesting performance of this hydroelastic system. Power extraction from an FIV-based device is typically implemented through a generator that acts as a damper with the power coefficient of the fluid-flow energy harvesting device defined by

$$C_P = P/(\frac{1}{2}\rho U^3 DL), \quad (6)$$

where the instantaneous power output is given by $P = F_y \dot{y}$. This measures the conversion of the flow energy passing across a cylinder diameter into extractable energy. Assuming the body vibration is periodic, the power output of a damper can be approximated by $P = c\dot{y}^2$. Typically, the power extraction performance is assessed by its temporal-average power coefficient over a period time (usually over many vibration cycles):

$$\bar{C}_P = \frac{1}{t} \int_0^t C_P(t) dt. \quad (7)$$

In principle for an FIV-based harvester, the energy extraction process is driven by the fluctuating force component, and the power output is determined by the product of the driving force and the body velocity ($P = F_y \dot{y}$). Thus, the possible maximum power output can be assessed through experiments with various damping settings that affect the dynamics of the hydroelastic system. Figure 7 shows the root-mean-square coefficient of the lift (C_y^{rms}) and the mean power output coefficient as a function of U^* . As can be seen, the peak value of C_y^{rms} is observed to be 2.8 for the case of $\zeta = 0.0032$, greater than twice that of its nonrotating counterpart. Similar to the body vibration amplitude, the C_y^{rms} peak decreases significantly to 2.1 when ζ is increased to 0.0182 ($G = 10.50$ mm). At this ζ value, the rotating cylinder of $\alpha = 2.0$ has a maximum power coefficient of $\bar{C}_P = 0.195$ (at $U^* = 6.1$ and $\text{Re} = 2150$), 13% higher than that of 0.173 (at $\zeta = 0.0345$, $G = 7.50$ mm, $U^* = 5.5$, and $\text{Re} = 2240$) of all nonrotating cases over the U^* range tested. Note that this maximum \bar{C}_P agrees with that measured with a lower mass ratio of 3.0 by Wang *et al.* [4]. On the other hand, however, for a given ζ value, \bar{C}_P values in the lower branch of the rotating cases appear to be considerably lower than those of their nonrotating counterparts. Overall, the above results suggest that the enhancement of the energy harvesting performance is considerably limited within the upper-branch regime, even without considering the power input to provide the imposed body rotation, as the fluctuating component of the lift can be attenuated significantly by increases in ζ .

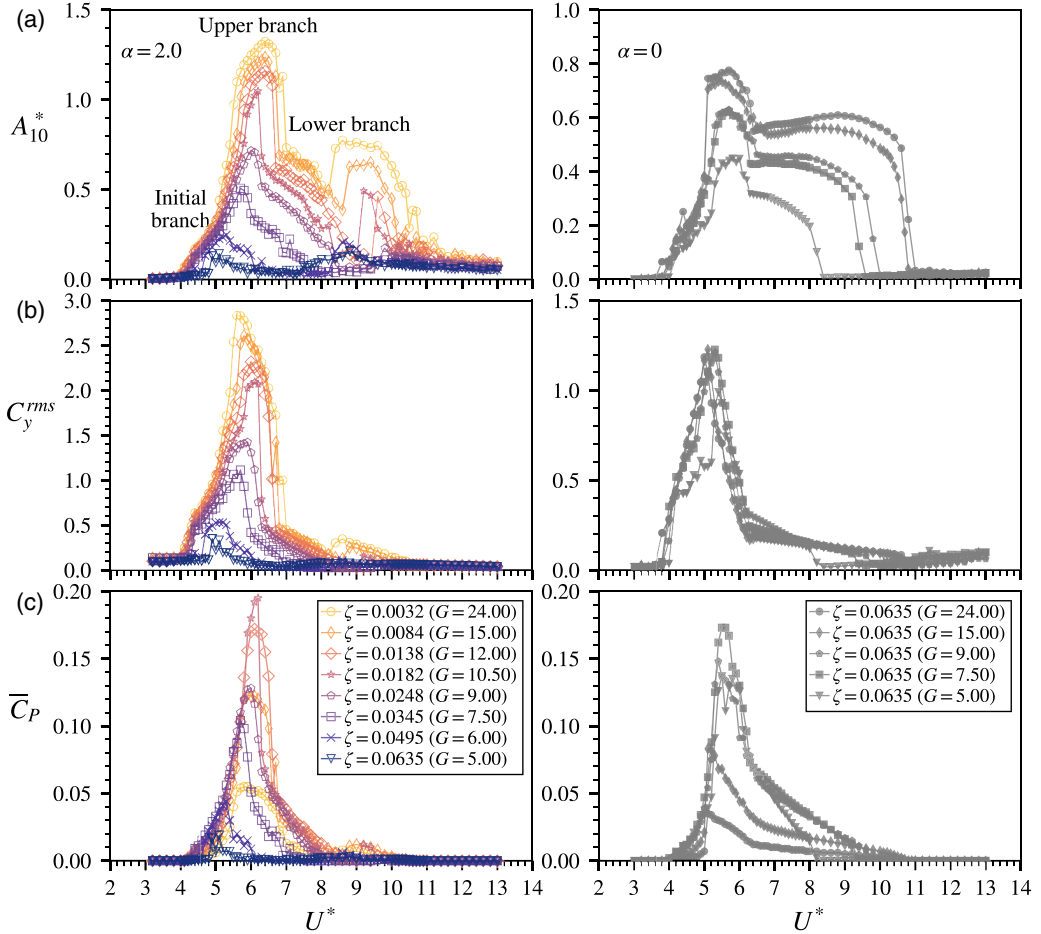


FIG. 7. Variations of the root-mean-square (rms) lift coefficient and the mean power coefficient as a function of reduced velocity at $\alpha = 2.0$ (in the left column) with various damping ratios, along with a comparison against selected nonrotating cases (in the right column). Panel (a) revisits the A_{10}^* responses for convenience of data presentation.

B. Dynamical response as a function of imposed rotation rate

In this subsection, we investigate the dynamical response as a function of α and ζ . This investigation covers a wide parameter space: $0 \leq \alpha \leq 3$ and $0.0032 \leq \zeta \leq 0.0635$, for three different reduced velocities: $U^* = 4.5, 6.0, \text{ and } 7.5$ (correspondingly, $\text{Re} = 1580, 2110, \text{ and } 2630$), as representatives selected from the initial, upper, and lower branches, respectively.

Figure 8 shows the variations of A_{10}^* , \bar{y}^* , \bar{C}_y , C_y^{rms} , and \bar{C}_P [in rows (i)–(v)] as a function of α for various ζ values at the three selected U^* values [in columns (a)–(c)]. As can be seen in Fig. 8, the damping effect has minimal influence on the A_{10}^* - α curves at $U^* = 4.5$ (the initial branch), while it can strongly affect the responses for $U^* = 6.0$ and 7.5 , as evidenced by the shrinking of the amplitude responses and the onset α for full suppression shifting to lower values with increasing ζ . On the other hand, as shown in Figs. 8(ii) and 8(iii), for a given U^* , changes in ζ have a negligible influence on the variations of \bar{y}^* and \bar{C}_y over the α range tested, except the range $1.5 < \alpha < 2.5$, where marginal deviations from their global trends (highlighted by the blue solid lines) are encountered with enhanced large-amplitude body oscillations due to strong fluid-structure interaction. It should be noted that in the \bar{y}^* - α plots, the blue solid line represents the \bar{y}^* value

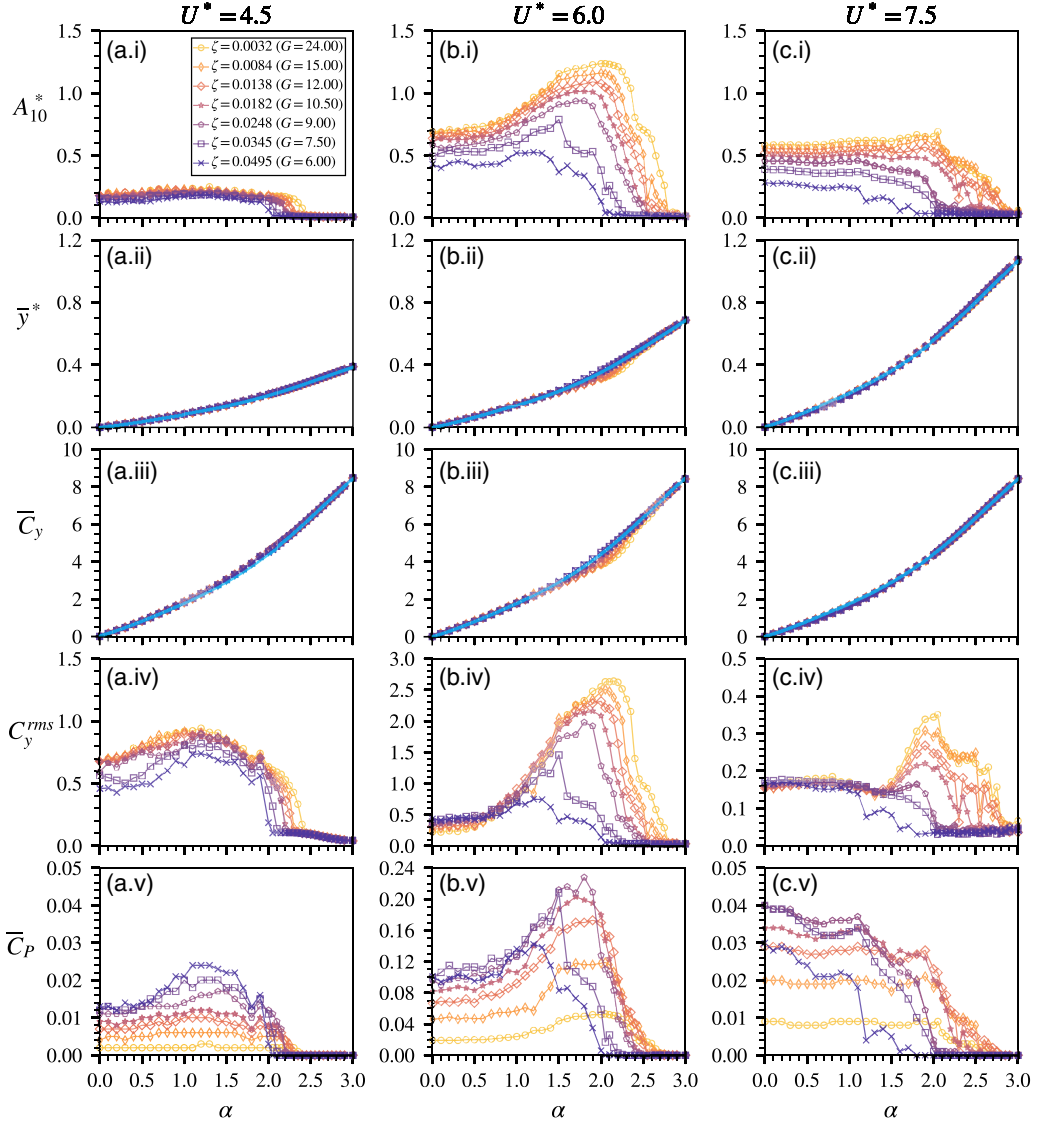


FIG. 8. Variations of A_{10}^* , \bar{y}^* , \bar{C}_y , C_y^{rms} , and \bar{C}_p as a function of α for various damping ratios at three representative reduced velocities, $U^* = 4.5, 6.0,$ and 7.5 . In row (ii), the blue lines represent the \bar{y}^* values evaluated using Eq. (5) with \bar{C}_y obtained from a fifth-order polynomial curve fit represented by the blue lines through all measurement cases in row (iii).

evaluated based on Eq. (5) with \bar{C}_y obtained from a fifth-order polynomial curve fit through all measurements of the three U^* cases, which, in turn, is represented by the blue solid line in the \bar{C}_y - α plots. The choice of this fifth-order polynomial fitting was adopted from that used for a wider α range by Zhao *et al.* [25]. With the results presented in Fig. 4(c), this confirms that \bar{C}_y predominantly depends on α over the U^* , and thus the Re, ranges tested.

Moreover, similar to the A_{10}^* responses, increases in ζ lead to significant reductions in the magnitude of C_y^{rms} for the cases of $U^* = 6.0$ and 7.50 , particularly over the range $1 < \alpha < 2.3$, where rotation-enhanced amplitudes tend to be encountered, as shown in Fig. 8(iv). On the other

hand, as shown in Fig. 8(b.v), \overline{C}_P tends to increase with ζ increased to 0.0248 ($G = 9.00$ mm), prior to a rapid decrease at a higher ζ value. The maximum of C_P is observed to be 0.230 at $\alpha = 1.8$, a 33% increase against the nonrotating cylinder ($\overline{C}_P = 0.173$). However, enhancements of the \overline{C}_P peak against the nonrotating case are observed to be limited within a narrow range of $1.5 \leq \alpha \leq 2.0$.

C. Wake structures and fluid forcing phases

In this subsection, we investigate the wake modes captured using PIV at the three representative velocities, $U^* = 4.5, 6.0,$ and 7.5 , for $\alpha = 2.0$ at various ζ values. Since a comprehensive wake mode map for flow past a rotating cylinder with low damping over a wide U^* - α parameter space has been given by Wong *et al.* [19], we focus here on how the wake modes vary at the three representative reduced velocities as ζ is increased.

Figure 9 shows snapshots of phase-averaged wake modes at $U^* = 4.5, 6.0,$ and 7.5 in columns (a)–(c), for $\alpha = 2$ at $\zeta = 0.0032, 0.0182, 0.0248,$ and 0.0345 (corresponding to $G = 24.00, 10.50, 9.00,$ and 7.50 mm, respectively) in rows (i)–(iv), together with the nonrotating case of $\zeta = 0.0345$ for comparison in row (v). Clearly, at $U^* = 4.5$ in the initial branch, the rotating cylinder exhibits a wake mode consisting of two single (S) vortices shed per body oscillation cycle. These vortices are shed downstream asymmetrically to the center line ($\tilde{y}^* = 0$) due to the body rotation effect, and thus this wake mode is referred to as an $A(2S)$ mode (see Ref. [19]), as opposed to the symmetric $2S$ mode introduced first by Williamson and Roshko [30]. This $A(2S)$ mode remains a well-defined pattern, despite the vorticity seeming to decay slightly as ζ is increased. It is interesting to note that this wake mode is associated with a wake-body synchronization characterized by both the body oscillation and vortex-shedding frequencies (f_y^* and $f_{C_y}^*$) matching f_{nw} in the initial branch for $\alpha = 2.0$, while the initial branch of a nonrotating cylinder is typically characterized by a “beating” dynamic behavior modulated by the vortex-shedding frequency and the natural frequency of the system (i.e., f_{nw}).

Further, at $U^* = 6.0$ in the upper branch, for $0.0032 \leq \zeta \leq 0.0248$ in Figs. 9(b.i)–9(b.iii), the wake pattern is identified as a $P^+ + S$ mode consisting of a pair of positive (P^+) anticlockwise-rotating (in red) vortices and a single negative clockwise-rotating (in blue) vortex shed per body oscillation cycle. It is interesting to note from Fig. 9(b.iii) that the case of $\zeta = 0.0248$ ($G = 9.00$ mm) still features a $P^+ + S$ mode as in the upper branch of other lower ζ cases, despite the lack of a clear jump in the amplitude response from the initial to the upper branch. The $P^+ + S$ mode in the upper branch of $\alpha = 2.0$ is observed to be stable, distinctly different from the $2P_o$ mode observed in the nonrotating cases, which is a weak $2P$ mode comprised of two pairs of opposite-sign vortices shed per cycle (see Refs. [7,8]). In fact, the experiments by Zhao *et al.* [9] showed that the upper branch of a nonrotating cylinder exhibits switching behavior between $2S$ and $2P_o$, due to the chaotic nature in the upper branch of VIV. With ζ further increased to 0.0345 ($G = 7.50$ mm), the wake mode is characterized by an $A(2S)$ pattern. A well-defined $A(2S)$ was also observed at a lower reduced velocity of $U^* = 5.6$ (not shown here). These results suggest that the upper branch disappears in this ζ case, in line with the A_{10}^* response in Fig. 4(a) showing that the cylinder rotation of $\alpha = 2.0$ exerts attenuation rather than enhancement effects for $\zeta \geq 0.0345$.

At $U^* = 7.5$, for the case of $\zeta = 0.0032$, a $P + P_o$ wake mode is observed. This wake mode consists of a pair of opposite-signed vortices (lower) shed in one half cycle and another opposite-signed pair (upper) in the other half cycle. As illustrated in Fig. 9(c.i), the upper pair is found to be a P_o pattern, as it has a weak positive vortex, which dissipates rapidly to make the wake appear as $P + S$. It should be noted that this mode was identified as a $P + S$ mode in Ref. [19] due to a lower resolution for phase averaging (8 phases), while the present study used more data and 48 phases to capture rapid changes in the wake structure for high rotation rates. The vortices in this wake mode break down rapidly as they travel downstream. This wake mode is distinctly different from the stable $2P$ mode observed in the lower branch of the nonrotating case in Fig. 9(c.v). Indeed, this wake mode is associated with a second harmonic in the lower branch, where the dynamics seem to be susceptible to changes in ζ . When ζ is increased to 0.0345 and the amplitude response falls

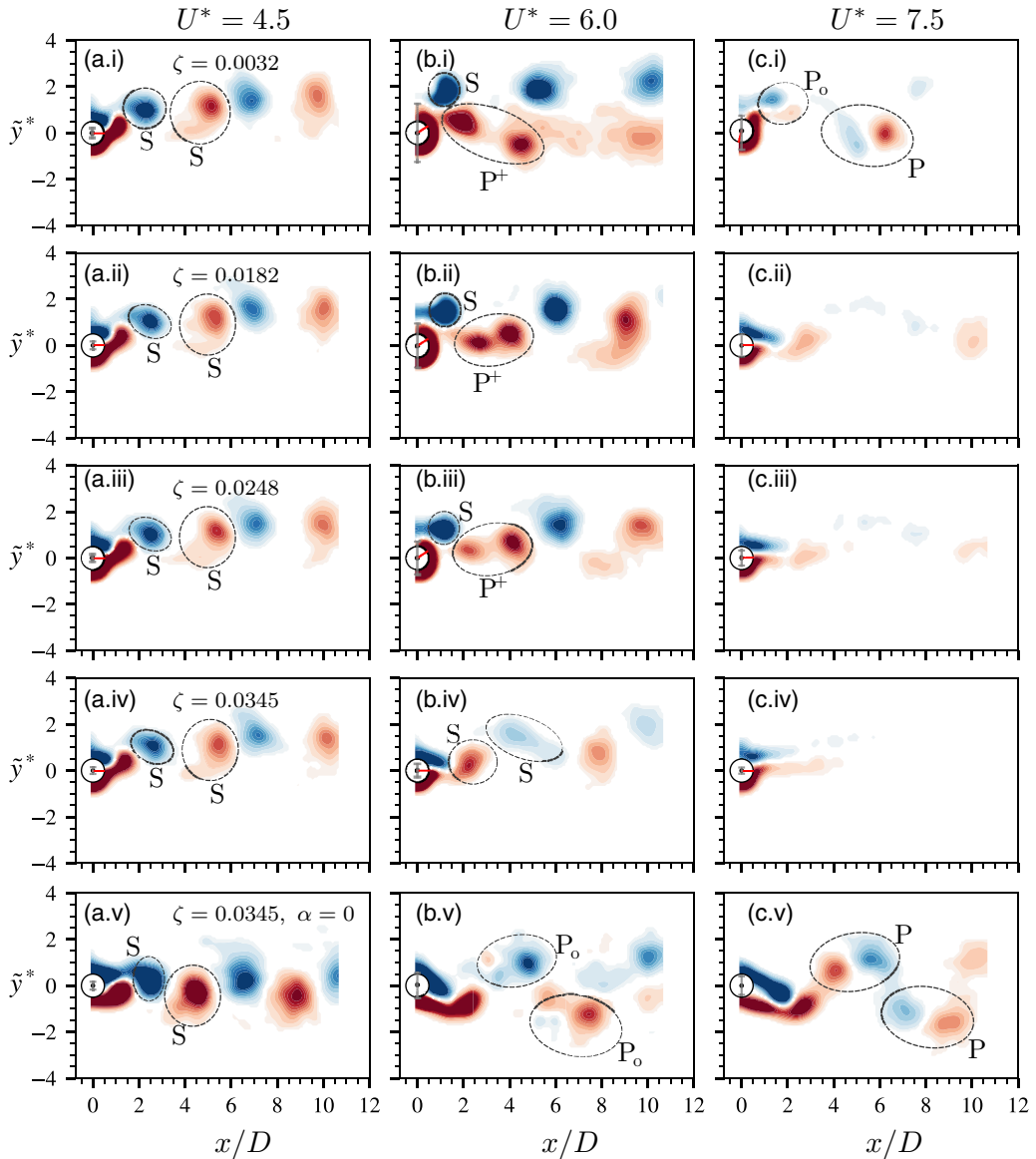


FIG. 9. Wake modes measured at three representative reduced velocities, $U^* = 4.5, 6.0$, and 7.5 in columns (a)–(c), respectively, for $\alpha = 2.0$ with four different damping ratios in rows (i)–(iv), as compared with the nonrotating cylinder with $\zeta = 0.0345$ in row (v). Note that \tilde{y}^* denotes the normalized fluctuating component of the body displacement, namely, $\tilde{y}^* = (y - \bar{y})/D$. The normalized vorticity range is $\omega_z^* = \omega_z D/U \in [-2, 2]$, where ω_z is the vorticity out of the x - y plane. The red and blue contours represent positive and negative vorticities, respectively. The gray bars indicate that the body vibration amplitude, and the red lines indicate the averaged phase angle of the PIV snapshots. Note that P^+ denotes a pair of positive vortices rotating in the anticlockwise direction, while P_o denotes a pair of opposite-sign vortices.

into the V-shape desynchronization region, as shown in Fig. 9(c.iv), the wake is characterized by a coalescence of small asymmetric vortices, which has been termed a $C(AS)$ mode by Wong *et al.* [19], rather than regular well-defined vortices.

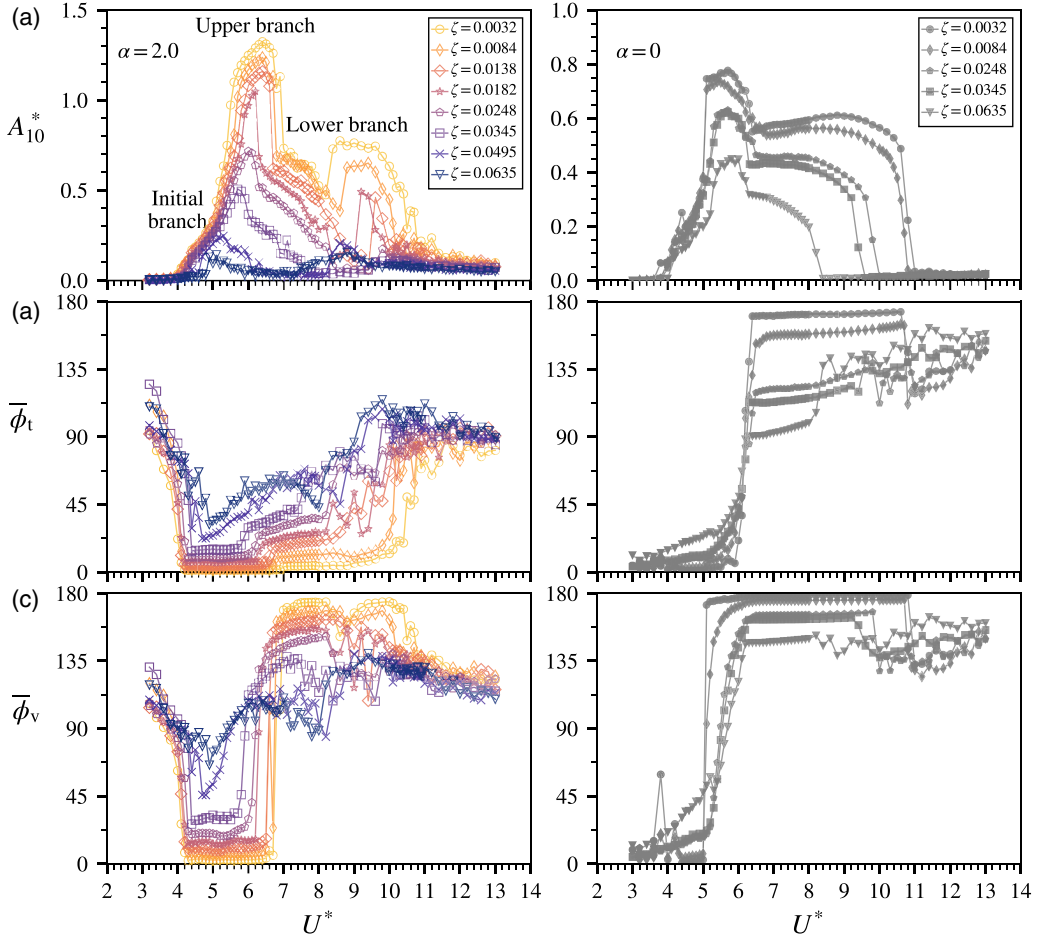


FIG. 10. The time-averaged total and vortex phases (in degrees) as a function of U^* at $\alpha = 2.0$ (in the left column) with various ζ values, along with a comparison against selected nonrotating cases (in the right column). Panel (a) revisits the A_{10}^* responses for convenience of data presentation.

The above PIV results show that the changes of the wake patterns for $\alpha = 2.0$ are in line with those of the amplitude response branches, due to the influence of the structural damping ratio. For the lightly damped cases (i.e., $\zeta \leq 0.0248$) with well-defined initial and upper branches, $A(2S)$ and $P^+ + S$ modes are consistently encountered in the initial and upper branches, respectively. When the upper branch is suppressed as ζ is increased to a certain value (i.e., $\zeta = 0.0345$ in the present experiments), an $A(2S)$ mode is observed to persist with appreciable but low body vibration amplitudes for U^* up to 7.5. On the other hand, the sensitivity of the lower branch to the influence of increasing structural damping ratios can also be reflected by the $P + P_o$ wake pattern being susceptible to the increases in the structural damping ratio, which breaks down much more easily than the $2P$ mode for the nonrotating cylinder case.

Furthermore, we examine the fluid forcing phases, namely, the total phase (ϕ_t) and the vortex phase (ϕ_v), which are referred to as the relative phase angles of total lift and vortex lift force, respectively, to the body displacement [7,31]. As has previously been reported (e.g., Refs. [7–9]), different wake modes could be related to different fluid forcing phases. Figure 10 plots the time-averaged phases of $\bar{\phi}_t$ and $\bar{\phi}_v$ as a function of U^* for both $\alpha = 2.0$ and $\alpha = 0$ with various ζ values. Typically in VIV of a nonrotating cylinder, $\bar{\phi}_t$ exhibits a sharp jump associated with the transition

from the upper branch to the lower branch, while $\bar{\phi}_v$ experiences a sharp jump in the transition from the initial branch to the upper branch. Distinctly different from the nonrotating cylinder, a sharp jump in $\bar{\phi}_v$ is encountered when the rotating cylinder undergoes the transition from the upper branch to the lower branch, while $\bar{\phi}_t$ remains around 45° , despite an increase trend with ζ . Unexpectedly, however, both $\bar{\phi}_t$ and $\bar{\phi}_v$ remain constant through the initial and the upper branches in each case of $\zeta \leq 0.0345$ at $\alpha = 2.0$, despite different wake modes occurring in the two branches. Nevertheless, the results of the wake modes and fluid forcing phases have revealed that the three branches of $\alpha = 2.0$ are associated with mechanisms different than those for the nonrotating cylinder.

IV. CONCLUSIONS AND RECOMMENDATIONS

We have investigated the damping effect on the transverse flow-induced vibration of a rotating cylinder through extensive experiments covering a wide parameter space across a reduced velocity range of $3 \leq U^* \leq 14$, a rotation rate range of $0 \leq \alpha \leq 3$, and a damping ratio range of $0.0032 \leq \zeta \leq 0.0635$. FIV characteristics, including the structural vibration, fluid forces and phases, and wake modes were examined in detail.

For the FIV response as a function of U^* at $\alpha = 2.0$, an enhanced three-branch amplitude response was encountered for $\zeta \leq 0.0182$, while for higher ζ values the cylinder rotation resulted in a reduced vibration amplitude response over the nonrotating case. The enhanced amplitude response seemed to be more susceptible to increases in ζ , as compared with the nonrotating counterpart. Moreover, unlike the nonrotating case, the lower branch seemed to be sensitive to changes in ζ , where a (repeatable) V-shape drop associated with a desynchronization was encountered at approximately $U^* = 8$ in the middle of the branch. By analyzing the frequency responses, we found that the lower branch was associated with a second harmonic component in the lift force signal, distinctly different from the third harmonic component observed for the nonrotating case. Furthermore, our targeted PIV measurements illustrated that the initial branch was associated with an $A(2S)$ mode, the upper branch with a $P^+ + S$ mode, and the lower branch with a $P + P_o$ mode. Both these results suggest that FIV of a rotating cylinder at $\alpha = 2.0$ is driven by mechanisms of fluid-structure interaction different from those observed for the nonrotating cylinder, despite the existence of a similar three-branch response.

Quantification of the transverse lift coefficient indicates that the time-averaged lift coefficient \bar{C}_y predominantly depends on α over the Reynolds number range ($1130 \leq Re \leq 5260$) tested, and the time-averaged body displacement can be well predicted based on \bar{C}_y and U^* , except for the regimes associated with large-amplitude oscillations. On the other hand, similar to the amplitude response, the fluctuating component (i.e., the root-mean-square coefficient) of the lift was found to be susceptible to increases in the structural damping ratio. Overall, in terms of energy harvesting performance, the power output coefficient \bar{C}_p was found to be enhanced by cylinder rotation within a limited range of $1.5 \leq \alpha \leq 2.0$, discounting the power input required for driving the imposed rotation. This suggests that a constantly rotating cylinder is perhaps not an ideal candidate for fluid flow energy harvesting.

ACKNOWLEDGMENTS

J.Z. gratefully acknowledges the support for his research fellowship from the Australian Research Council (ARC) through a Discovery Early Career Research Award (Grant No. DE200101650). The authors also gratefully acknowledge the ARC funding support through Discovery Project Grants No. DP190103388, No. DP200100704, and No. DP210100990.

[1] P. H. N. Brooks, Experimental investigation of the aeroelastic instability of bluff two-dimensional cylinders, M.A.Sc. thesis, University of British Columbia, 1960.

- [2] M. M. Bernitsas, K. Raghavan, Y. Ben-Simon, and E. Garcia, VIVACE (Vortex Induced Vibration Aquatic Clean Energy): A new concept in generation of clean and renewable energy from fluid flow, *J. Offshore Mech. Arct. Eng.* **130**(4), 041101 (2008).
- [3] Z. Wang, L. Du, J. Zhao, and X. Sun, Structural response and energy extraction of a fully passive flapping foil, *J. Fluids Struct.* **72**, 96 (2017).
- [4] A. K. Soti, J. Zhao, M. C. Thompson, J. Sheridan, and R. Bhardwaj, Damping effects on vortex-induced vibration of a circular cylinder and implications for power extraction, *J. Fluids Struct.* **81**, 289 (2018).
- [5] J. Wang, L. Geng, L. Ding, H. Zhu, and D. Yurchenko, The state-of-the-art review on energy harvesting from flow-induced vibrations, *Appl. Energy* **267**, 114902 (2020).
- [6] A. Khalak and C. H. K. Williamson, Dynamics of a hydroelastic cylinder with very low mass and damping, *J. Fluids Struct.* **10**, 455 (1996).
- [7] R. Govardhan and C. H. K. Williamson, Modes of vortex formation and frequency response of a freely vibrating cylinder, *J. Fluid Mech.* **420**, 85 (2000).
- [8] T. L. Morse and C. H. K. Williamson, Prediction of vortex-induced vibration response by employing controlled motion, *J. Fluid Mech.* **634**, 5 (2009).
- [9] J. Zhao, J. S. Leontini, D. Lo Jacono, and J. Sheridan, Chaotic vortex induced vibrations, *Phys. Fluids* **26**, 121702 (2014).
- [10] A. Nemes, J. Zhao, D. Lo Jacono, and J. Sheridan, The interaction between flow-induced vibration mechanisms of a square cylinder with varying angles of attack, *J. Fluid Mech.* **710**, 102 (2012).
- [11] J. Zhao, J. S. Leontini, D. Lo Jacono, and J. Sheridan, Fluid–structure interaction of a square cylinder at different angles of attack, *J. Fluid Mech.* **747**, 688 (2014).
- [12] J. Zhao, K. Hourigan, and M. C. Thompson, Flow-induced vibration of D-section cylinders: an afterbody is not essential for vortex-induced vibration, *J. Fluid Mech.* **851**, 317 (2018).
- [13] J. Zhao, A. Nemes, D. Lo Jacono, and J. Sheridan, Branch/mode competition in the flow-induced vibration of a square cylinder, *Philos. Trans. R. Soc. London, Ser. A* **376**, 20170243 (2018).
- [14] E. G. Reid, Tests of rotating cylinders, NACA Technical Notes 209, 1924.
- [15] L. Prandtl, Application of the “Magnus effect” to the wind propulsion of ships, NACA Technical Memorandum 367, 1926.
- [16] D. Stojković, P. Schön, M. Breuer, and F. Durst, On the new vortex shedding mode past a rotating circular cylinder, *Phys. Fluids* **15**, 1257 (2003).
- [17] S. Mittal and B. Kumar, Flow past a rotating cylinder, *J. Fluid Mech.* **476**, 303 (2003).
- [18] A. Radi, M. C. Thompson, A. Rao, K. Hourigan, and J. Sheridan, Experimental evidence of new three-dimensional modes in the wake of a rotating cylinder, *J. Fluid Mech.* **734**, 567 (2013).
- [19] K. W. L. Wong, J. Zhao, D. Lo Jacono, M. C. Thompson, and J. Sheridan, Experimental investigation of flow-induced vibration of a rotating circular cylinder, *J. Fluid Mech.* **829**, 486 (2017).
- [20] R. Bourguet and D. Lo Jacono, Flow-induced vibrations of a rotating cylinder, *J. Fluid Mech.* **740**, 342 (2014).
- [21] R. Bourguet and D. Lo Jacono, In-line flow-induced vibrations of a rotating cylinder, *J. Fluid Mech.* **781**, 127 (2015).
- [22] L. Du and X. Sun, Suppression of vortex-induced vibration using the rotary oscillation of a cylinder, *Phys. Fluids* **27**, 023603 (2015).
- [23] B. Seyed-Aghazadeh and Y. Modarres-Sadeghi, An experimental investigation of vortex-induced vibration of a rotating circular cylinder in the crossflow direction, *Phys. Fluids* **27**, 067101 (2015).
- [24] K. W. L. Wong, J. Zhao, D. Lo Jacono, M. C. Thompson, and J. Sheridan, Experimental investigation of flow-induced vibration of a sinusoidally rotating circular cylinder, *J. Fluid Mech.* **848**, 430 (2018).
- [25] J. Zhao, D. Lo Jacono, J. Sheridan, K. Hourigan, and M. C. Thompson, Experimental investigation of in-line flow-induced vibration of a rotating cylinder, *J. Fluid Mech.* **847**, 664 (2018).
- [26] R. Bourguet, Impact of body inclination on the flow past a rotating cylinder, *J. Fluid Mech.* **923**, A33 (2021).
- [27] A. Sareen, J. Zhao, D. Lo Jacono, J. Sheridan, K. Hourigan, and M. C. Thompson, Vortex-induced vibration of a rotating sphere, *J. Fluid Mech.* **837**, 258 (2018).

- [28] A. Sareen, J. Zhao, J. Sheridan, K. Hourigan, and M. C. Thompson, The effect of imposed rotary oscillation on the flow-induced vibration of a sphere, *J. Fluid Mech.* **855**, 703 (2018).
- [29] T. McQueen, J. Zhao, J. Sheridan, and M. Thompson, Feedback control of flow-induced vibration of a sphere, *J. Fluid Mech.* **889**, A30 (2020).
- [30] C. H. K. Williamson and A. Roshko, Vortex formation in the wake of an oscillating cylinder, *J. Fluids Struct.* **2**, 355 (1988).
- [31] J. Lighthill, Fundamentals concerning wave loading on offshore structures, *J. Fluid Mech.* **173**, 667 (1986).